

Impact analysis of multiple parameters on fracture formation during volume fracturing in coalbed methane reservoirs

Tingting Jiang, Jianhua Zhang* and Hao Wu

Hubei Province Key Laboratory of Processing of Mineral Sources and Environment, School of Resource and Environmental Engineering, Wuhan University of Technology, Wuhan 430070, Hubei, China

Uniaxial and triaxial compression, Brazilian splitting and three-point bending tests have been carried out to determine the mechanical parameters of the coal reservoir in Jiaozuo coal mining district, Henan Province, China. Based on the experimental results and combined with the target reservoir geological characteristics, a 3D geological mechanical model has been established to analyse the hydraulic fracture propagation during volume fracturing using MEYER software. Effects of the modulus of coal rock, difference between horizontal principal stresses, fracturing fluid viscosity and fracturing fluid injection rate on the fracturing network geometry are studied. Results show that fracturing network development intensity in the coalbed methane (CBM) reservoir is determined both by the geological conditions and the hydraulic fracturing parameters. The intensity of fracturing in the CBM reservoir is positively related with the elastic modulus of the coal rock, and is inversely proportional to the difference between the two horizontal principal stresses. Increasing fluid viscosity reduces the fracturing area. Low injection rate is beneficial to improving hydraulic treatment areas when it is larger than that required to guarantee that the crack extends. The results can provide a case reference for optimization design of volume fracturing and productivity prediction analysis of CBM reservoirs.

Keywords: Coalbed methane reservoir, fracture network, numerical simulation, volume fracturing.

IN volume fracturing, the resulting fracture network geometry is mainly determined by the *in situ* stress and rock physical and mechanical properties (elastic modulus, Poisson ratio, tensile strength and fracture toughness). In addition, the fracturing implementation parameters (such as construction scale, capacity, viscosity and filtration of fracturing fluid, etc.) affect fracture geometry to a certain extent^{1,2}. Coalbed methane (CBM) reservoirs contain a large number of pores³, which make the fracture geometry more complicated. The analysis of fracture network geometry can guide an efficient exploitation of CBM and

be of significance on the later evaluation of fracturing effectiveness^{4,5}.

Volume fracturing as a new kind of fracturing technology is totally different from conventional hydraulic fracturing. It makes full use of the formation bedding and natural fractures to produce a number of transverse and longitudinal artificial fractures which communicate with the natural fracture system away from the wellbore. It is intended to further expand the discharge area, rather than to control the expansion of natural fractures^{6,7}. The volume fracturing technology will most likely communicate further natural fractures and form a larger seepage scope^{8,9}. It will exert the advantages of the natural fracture network to increase production and enhance matrix supply capacity. It will also improve the stimulation effect and have importance in unconventional reservoir recovery.

Coal rock mechanics parameters are the prerequisites of CBM reservoir hydraulic fracture prediction, and also help understand the law of crack propagation^{10,11}. Since coal contains several developed joints and fissures, which have a major influence on mechanical performance, the differences in mechanical parameters are large between different regions and formations¹².

Injection pressure and elastic modulus of coal had control effects on hydraulic fracturing propagation¹³. The authors proposed that fracturing fluid viscosity had a limited effect on the fracture propagation. Li *et al.*¹⁴ studied the effects of the mechanical property (*in situ* stress, elastic modulus and permeability, etc.) differences between adjacent layers and fracturing fluid parameters (injection rate, viscosity, proppant size, etc.) on hydraulic fracture propagation along the vertical direction of the formation. The mechanical properties of stratum had a major influence on the fracture extension. Stress sensitivity, comprehensive filtration coefficient and pumping delivery capacity were the key factors affecting the fracture length¹⁵. Klawitter *et al.*¹⁶ analysed the fractures resulting in coal using the shore scleroscope rebound hardness test, which can be scaled up to understand fracture propagation in CBM reservoirs. Li and Xing¹⁷ studied the effect of formation properties on the hydraulic fracture initiation. They argued that hydraulic fracture could initiate earlier if the values of permeability, porosity, Young's

*For correspondence. (e-mail: zjhwt@sina.com)

modulus and Poisson ratio were higher, when the hydraulic pressure was a constant. Kirk-Burnnand *et al.*¹⁸ reached a conclusion similar to that of Li and Xing¹⁷. They further concluded that reservoir complexity was mainly impacted by the lateral continuity variations of coal seams. Dehghan *et al.*¹⁹ confirmed that the pre-existing fractures around the wellbore could reduce the effect of the original stress concentration, which led to a drastic decrease of fracture initiation and propagation pressure. With the increase of horizontal *in situ* stress difference, the fracture propagation changed from a single fracturing mode to a multiple fracture mode. Ma *et al.*²⁰ studied the effect of the direction of minimum principal stress and the difference between maximum and minimum horizontal stresses on hydraulic fracture propagation. They confirmed that the two factors have notable effects on the fracturing pattern.

However, the studies mentioned above were mainly based on the assumption that the coal seam was homogeneous. Researchers did not take the bedding into consideration. Bedding is one of the main aspects of coal seams. Their mechanical parameters differ greatly from those of the adjacent strata. The bedding distribution patterns of coal seam are variable (such as horizontal, wavy and inclined bedding), which results in heterogeneity of the mechanical properties²¹. These factors make the parameters of coal highly inconsistent in different areas; so it is of great significance to carry out tests to determine their parameters to predict hydraulic fracture extension.

Laboratory experiments have been carried out to determine the mechanical properties of Shanxi Formation in Henan Province, China. According to the target reservoir geology characteristics, a 3D mechanical model of the fracture network extension was built using MEYER²². The model was used to analyse the influence of elastic modulus, differences in horizontal principal stresses, fracturing fluid viscosity and injection rate on the fracture network formed in the CBM reservoir. Results can provide a reference basis for volume fracturing optimization design and productivity prediction analysis of CBM reservoirs.

Experimental analysis

In order to obtain raw coal of the target coal seam deep underground of the Shanxi Formation, we used blast mining at the target layer after coal mine roadway was completed. The large raw coal blocks obtained by blasting were transported to the surface from the roadway. In order to lessen the influence of buried depth differences of coal samples and improve the reliability of test results, raw coal should be sampled at the same position as far as possible. In the process of carrying raw coal to the surface, severe vibration was avoided to prevent damage to the structure. Figure 1 shows a large raw coal carried to

the surface. The raw coal was packaged hermetically and put in a wooden case with anti-vibration protection: plastic foam was placed between raw coal and the box walls to prevent collision. The raw coal was transported quickly to the laboratory for processing.

To obtain the mechanical parameters of coal rocks, we carried out uniaxial and triaxial compression tests, Brazilian splitting test and three-point bending test on rock samples from the target reservoir. Because of the anisotropy of the coal, the angles between drilling direction and bedding plane were selected as 0° and 90°. Figure 2 *a* shows the site coring process. Figure 2 *b* shows a schematic diagram of the directional coring, where the dashed line indicates bedding. Water cutting was used to core samples from the coal blocks. The samples were polished by hand to meet the requirements of test standards^{23,24}.

The standard cylindrical specimens used in uniaxial and triaxial compression tests have the diameter and height of 50 and 100 mm respectively. The diameter and height of Brazilian splitting test samples are 50 and 25 mm respectively. The specimen size of three-point bending test is $\phi 50 \times 200$ mm. The flatness error of sample faces is controlled within 0.03 mm, and the size error is not greater than 0.5 mm. The two end faces must be perpendicular to the specimen axis, and the largest deviation angle should be no more than 0.25°. Every sample was packed in plastic wrap immediately after processing and a detailed record label was made. Figure 3 shows the standard coal samples.

We used the multifunctional rock testing system (RMT) (Figure 4) to carry out the compression tests, Brazilian splitting test and three-point bending test.



Figure 1. Raw coal carried to the surface.

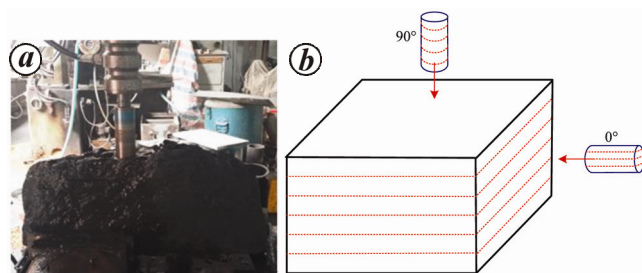


Figure 2. Coring diagram. *a*, Site coring process; *b*, Directional coring.

Uniaxial compression test

For uniaxial compressive strength test, the samples were divided into two groups based on their orientation. Each set of tests was performed on at least three samples, and the average of the test results was taken. Cylindrical specimens were placed in a rubber sleeve before loading. The specimen was preloaded when the deformation sensor and signal receiver were connected. We adopted displacement control mode and the loading rate was maintained at 0.002 mm/s until the specimen failed.



Figure 3. Standard coal samples.



Figure 4. Multifunctional rock testing system.

The uniaxial compressive strength of coal samples can be obtained by

$$\sigma_{ac} = (P/A), \quad (1)$$

where σ_{ac} is the uniaxial compressive strength, Pa; P the ultimate load, N and A is the cross-sectional area, m^2 .

The stress–strain curve of uniaxial compressive test can be described with the ordinate and abscissa of longitudinal stress and strain respectively. The computational formula of elasticity modulus is shown as

$$E = (\Delta\sigma / \Delta\varepsilon), \quad (2)$$

where $\Delta\sigma$ and $\Delta\varepsilon$ are the longitudinal stress increment and longitudinal strain increment of the straight segment respectively.

Poisson ratio is obtained by

$$\mu = (\varepsilon_{2p} / \varepsilon_{1p}), \quad (3)$$

where ε_{1p} is the strain average value of straight segment in longitudinal stress and longitudinal strain curve. While ε_{2p} is the strain average value of straight segment in longitudinal stress and transverse strain curve.

Table 1 shows the test results. The angle between coring direction and bedding plane has a major influence on coal rock compressive strength and elastic modulus. Compressive strength is much larger when the coring angle is 90° . However, the difference in Poisson ratio mean value is just 0.03.

Figure 5 shows typical failure patterns at different coring angles. When the coring angle is 0° , tensile fracturing takes place along the bedding with multiple tension fracture planes parallel to the bedding and a breakthrough on both ends. Samples show complex tension splitting and shear failures, and break easily into pieces when the coring angle is 90° .

Table 2 shows the uniaxial compression parameters of bedding and matrix.

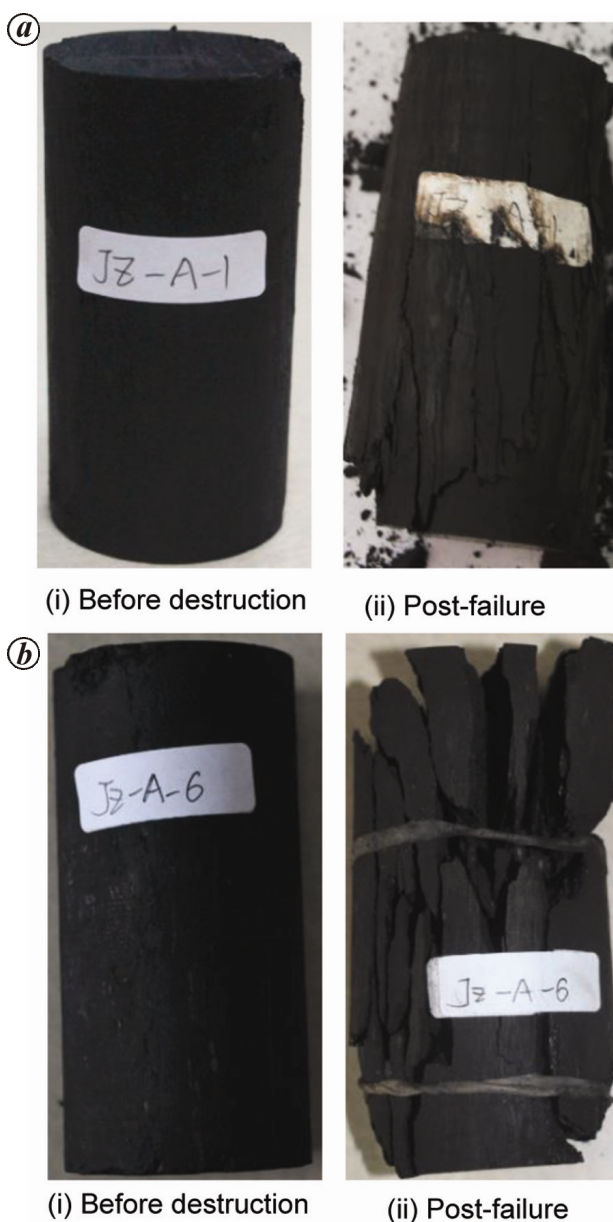
Triaxial compression test

The triaxial compression tests use the axial displacement control mode with loading rate of 0.002 mm/s. Confining pressure was increased to the predetermined value at a rate of 0.1 MPa/s. Then axial load was applied until destruction of the sample.

The coring angles remained at 0° and 90° for the triaxial compression tests. The confining pressures were 1, 2, 3, 4 and 5 MPa. Each group under the same confining pressure consisted of at least three samples, and then the average value was taken. Tables 3 and 4 show coal rock triaxial compression test results at different bedding angles.

Table 1. Test results of uniaxial compression

Sample number	Coring angle (°)	Sample size (mm)		Compressive strength (MPa)	Elasticity modulus (GPa)	Poisson ratio
		Diameter	Height			
JZ-A-1	0	49.83	99.84	3.20	0.70	0.37
JZ-A-2		49.76	99.70	3.27	0.64	0.27
JZ-A-3		49.70	99.73	2.70	0.61	0.38
Mean value		49.76	99.76	3.06	0.65	0.34
JZ-A-4	90	49.80	99.84	12.32	2.04	0.31
JZ-A-5		49.65	99.59	12.04	1.95	0.33
JZ-A-6		49.59	99.71	11.27	1.80	0.28
Mean value		49.68	99.71	11.88	1.93	0.31

**Figure 5.** Samples before and after uniaxial compression. *a*, Coring angle 0°; *b*, Coring angle 90°.**Table 2.** Coal rock uniaxial compression parameters

Lithology	Compressive strength (MPa)	Elastic modulus (GPa)	Poisson ratio
Matrix	11.88	1.93	0.31
Bedding	3.06	0.65	0.34

The test results show that triaxial compression strength is the largest when bedding angle is 90°. The compressive strength difference between different bedding angles decreases with increasing confining pressure. The confining pressure suppresses bedding shear slipping, such that increasing confining pressure reduces strength anisotropy. Figures 6 and 7 show typical triaxial compression fracture styles for different bedding angles.

With the increase of confining pressure, fracture energy increases until axial stress reaches the peak strength. Released elastic energy is insufficient to induce further damage. Coal specimen rupture mode basically shows two types of failure. (1) Conjugate shear failure, where there are two or more fracture planes in the samples, which can be divided into two groups parallel to each other. The two groups of failure surfaces cross through the sample and divide it into several blocks, eventually forming a conjugate shear fracture surface. The failure mode is of this kind (JZ-T-3-5 and JZ-T-3-4) when confining pressures are 1 and 2 MPa with coring angle 0°. (2) Single shear failure, where destroyed specimens all have one or two primary shear surfaces which in general go through both sample ends. When bedding angle is 90° or confining pressure is higher, a single shear failure develops, controlled by the matrix. Compared with uniaxial compression damage, the influence of bedding on failure pattern is reduced significantly in triaxial compression; however confining pressure has an increasing influence on failure pattern. Due to the effect of confining pressure, the damage form is no longer splitting failure, but shear failure.

The Mohr stress circle is drawn based on the triaxial compression test results. According to the Mohr–Coulomb

Table 3. Triaxial compression test results of bedding angle 0°

Sample number	Bedding angle (°)	Diameter (mm)	Height (mm)	Confining pressure (MPa)	Compressive strength (MPa)
JZ-T-3-5	0	49.53	99.72	1	6.762
JZ-T-4-5		49.55	99.58		6.177
JZ-T-5-5		49.64	99.53		6.054
Average value		49.57	99.61		6.331
JZ-T-3-4	0	49.61	99.80	2	12.133
JZ-T-4-4		49.59	99.50		11.697
JZ-T-5-4		49.75	99.63		10.886
Average value		49.65	99.64		11.572
JZ-T-3-3	0	49.77	99.87	3	16.652
JZ-T-4-3		49.64	99.51		15.309
JZ-T-5-3		49.92	100.12		15.216
Average value		49.78	99.83		15.726
JZ-T-3-2	0	49.48	99.66	4	19.726
JZ-T-4-2		49.82	99.76		18.337
JZ-T-5-2		49.75	99.54		19.590
Average value		49.68	99.65		19.218
JZ-T-3-1	0	50.12	99.67	5	24.451
JZ-T-4-1		49.81	99.73		22.789
JZ-T-5-1		49.69	100.06		24.082
Average value		49.87	99.82		23.774

Table 4. Triaxial compression test results of bedding angle 90°

Sample number	Bedding angle (°)	Diameter (mm)	Height (mm)	Confining pressure (MPa)	Compressive strength (MPa)
JZ-T-2-6	90	49.60	99.47	1	14.629
JZ-T-1-6		49.46	99.80		15.471
JZ-T-0-6		49.67	99.81		15.842
Average value		49.58	99.69		15.314
JZ-T-2-5	90	49.79	99.98	2	19.507
JZ-T-1-5		49.55	99.53		20.176
JZ-T-0-5		50.11	99.74		18.390
Average value		49.82	99.75		19.358
JZ-T-2-4	90	49.61	99.87	3	23.942
JZ-T-1-4		49.83	99.60		23.518
JZ-T-0-4		50.59	99.66		22.913
Average value		50.01	99.71		23.458
JZ-T-2-3	90	49.73	99.93	4	25.713
JZ-T-1-3		49.69	99.87		26.432
JZ-T-0-3		49.94	99.54		26.016
Average value		49.79	99.78		26.054
JZ-T-2-2	90	49.79	99.98	5	29.980
JZ-T-1-2		49.55	99.53		29.679
JZ-T-0-2		50.11	99.74		28.560
Average value		49.82	99.75		29.406

strength theory the triaxial compression characteristic parameters of matrix and bedding are determined which are shown in Table 5.

Brazilian disk splitting test

The axial displacement control mode in Brazilian splitting testing was used with the rate of 0.002 mm/s. Loading

was stopped after splitting failure developed. Brazilian splitting test samples were prepared with the disk plane parallel and perpendicular to the bedding. Figure 8 shows the Brazilian splitting test arrangement. We obtained the tensile strength of the matrix when the disk plane was parallel to the bedding (Figure 8a). Bedding angle is defined as the angle between bedding and loading direction (Figure 8b). To ensure accuracy of the test results, each

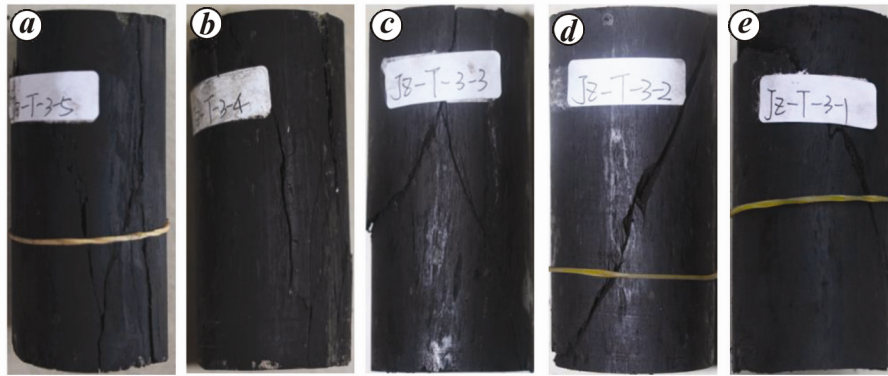


Figure 6. Coal triaxial compression fracturing shapes of bedding angle 0°. *a*, 1 MPa; *b*, 2 MPa; *c*, 3 MPa; *d*, 4 MPa; *e*, 5 MPa.

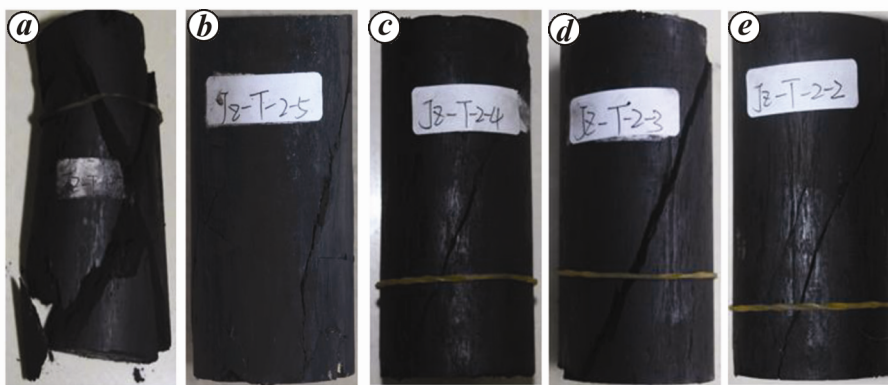


Figure 7. Coal triaxial compression fracturing shapes of bedding angle 90°. *a*, 1 MPa, *b*, 2 MPa, *c*, 3 MPa, *d*, 4 MPa; *e*, 5 MPa.

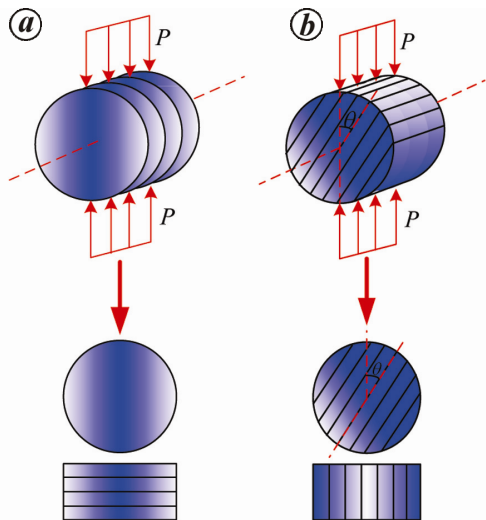


Figure 8. Schematic diagram of Brazilian disk splitting test. *a*, Parallel to bedding; *b*, Perpendicular to bedding.

Table 5. Coal rock triaxial compression characteristic parameters

Lithology	Internal friction angle (°)	Cohesive strength (MPa)
Matrix	18.8	0.82
Bedding	16.3	0.19

set of bedding angles was tested on at least three specimens. The average values were the tensile strengths for the corresponding bedding angles.

Tensile strength is given by²⁵

$$\sigma_t = (2P / \pi DH), \tag{4}$$

where σ_t (Pa) is the tensile strength, P (N) the ultimate load, D (m) the diameter of the sample and H (m) is the height of the sample.

Table 6 shows results of the Brazilian splitting test. The table shows that tensile strength is the largest (1.17 MPa) when the disk plane is parallel to the bedding, which indicates that the matrix has maximum tensile strength. The minimum tensile strength is 0.27 MPa, when the bedding angle is 0°, which indicates that the bedding is the weak interface of a CBM reservoir. Tensile strength improves significantly (to 0.54 MPa), when the bedding angle is 90°, but it is still less than the tensile strength of the matrix. This suggests that even when the loading direction is perpendicular to the bedding, the bedding still has some impact on the tensile strength and reduces it to a certain extent. The mean values of coal rock tensile strength are 0.54 and 0.27 MPa respectively, when bedding angles are 90° and 0°. The

Table 6. Test results of Brazilian splitting

Sample number	Bedding direction	Bedding angle (°)	Sample size (mm)		Tensile strength (MPa)	
			Diameter	Height	Trial value	Average value
JZ-BX-3	Parallel to disk	/	49.70	24.61	1.198	1.17
JZ-B2			49.69	24.53	1.175	
JZ-B3			49.54	24.89	1.138	
JZ-BX-2	Perpendicular to disk	90	49.54	24.78	0.553	0.54
JZ-BX-5			49.60	24.74	0.521	
JZ-B1			49.94	25.03	0.552	
JZ-BX-1	Perpendicular to disk	0	50.13	24.86	0.370	0.27
JZ-BX-4			49.75	24.91	0.271	
JZ-B4			49.83	24.56	0.168	

Table 7. Coal tensile strength characteristic parameters

Failure plane	Matrix	Bedding	Perpendicular to bedding
Tensile strength (MPa)	1.17	0.27	0.54



Figure 9. Splitting failure patterns of coal. *a*, Bedding parallel to disk surface; *b*, Bedding angle 90°; *c*, Bedding angle 0°.



Figure 10. Relative position of incision plane and bedding. *a*, Incision plane perpendicular to bedding; *b*, Incision plane parallel to bedding.

former is about twice the latter, which fully reflects the anisotropy of coal tensile strength.

Through the relationship between fracture surface, bedding and loading direction, we observed that failure patterns show large differences. Figure 9 shows Brazilian fracture shapes.

The vertical main fracture goes through the disc centre line and extends along the loading direction when bedding is parallel to the disc surface (Figure 9 *a*). Local bifurcation cracks develop near the lower load jaw, but the split cracks are short. When bedding angle is 90°, the vertical main fracture approximately passes through the

centre line of the disc and extends vertically to the bedding. The vertical main crack produces horizontal secondary cracks along the bedding direction. The tilted branch crack is generated at the centre of the disk, and finally forms complex fracture geometry (Figure 9 *b*). When the bedding angle is 0°, the vertical crack extends through the centre line of the sample along the bedding to form a relatively flat fracture (Figure 9 *c*).

Table 7 shows the tensile strength of matrix and bedding based on failure patterns.

Three-point bending test

Three-point bending test was carried out on the RMT testing machine with the specimen size of $\varnothing 50 \times 200$ mm. The axes of cylinder samples were parallel or perpendicular to the bedding respectively. Longitudinal notch form was adopted. Figure 10 shows the relative position of notch and bedding. In the figure, dotted lines represent the bedding, while depth and width of the notch are 20 and 1.5 mm respectively.

We must guarantee the accuracy of the specimen placement in the test fixture, and the notch centre line should be located right at the middle between the two supporting points (Figure 11). The notch opening displacement control mode was adopted with the rate of 0.0002 mm/s. In order to reduce the variability of test results, three-point bending tests were performed on at least three pieces in each group and the average of the test results was taken.

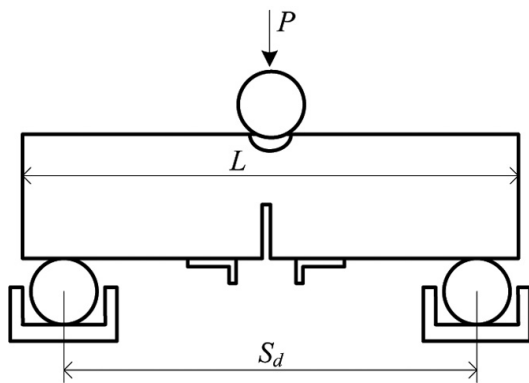
The formulas for calculating rock fracture toughness are

$$K_{IC} = 0.25 \left(\frac{S_d}{D} \right) \frac{P_{max}}{D^{1.5}} y \left(\frac{a}{D} \right), \quad (5)$$

$$y \left(\frac{a}{D} \right) = \frac{12.75 \left(\frac{a}{D} \right)^{0.5} \left[1 + 19.65 \left(\frac{a}{D} \right)^{4.5} \right]^{0.5}}{\left(1 - \frac{a}{D} \right)^{0.25}}, \quad (6)$$

Table 8. Test results of coal rock fracture toughness

Relative position of incision plane and bedding	Incision depth (mm)	Incision width (mm)	Diameter (mm)	Peak load (N)	Fracture toughness (MPa m ^{0.5})	Average value (MPa m ^{0.5})
Vertical	18.92	1.58	49.61	562.72	0.409	0.364
	20.73	1.63	49.74	479.43	0.385	
	19.44	1.46	50.38	421.07	0.298	
Parallel	20.38	1.55	50.21	145.90	0.111	0.120
	20.15	1.57	49.82	177.04	0.136	
	19.27	1.66	49.65	151.27	0.112	

**Figure 11.** Schematic diagram of three-point bending test.

where K_{IC} (Pa.m^{0.5}) is the fracture toughness, S_d the distance between the two supporting points and a constant of 160 mm is taken in three-point bending test, D (m) the sample diameter, P_{max} (N) the failure load and a (m) is the notch depth.

Based on eqs (5) and (6), fracture toughness does not affect the mechanical properties of the rock material. It is only related to sample size, notch geometry and the load. Table 8 shows results of coal fracture toughness test.

Thus, the angle between coring direction and bedding plane has a large influence on coal compressive strength and elastic modulus in uniaxial compression tests. The compressive strength of the coal matrix is 3.88 times larger than that of the bedding, while elastic modulus is about 2.97 times larger. The triaxial compression strength is the largest when the bedding angle is 90°. The compressive strength difference between different bedding angles decreases with increasing confining pressure. The cohesive strength of the matrix is 4.32 times larger than that of the bedding. Bedding has a major impact on the tensile strength based on the results of Brazilian splitting test, reduces the tensile strength to a certain extent. The mean tensile strength of matrix and bedding is 1.17 and 0.27 MPa respectively. The former is about 4.33 times larger than the latter, which fully reflects the anisotropy of coal tensile strength. Based on three-point bending test, fracture toughness also has strong anisotropy. It is about 3.03 times larger than that of the bedding.

Three-dimensional geomechanical simulation model of fracture propagation

In order to improve permeability and enhance the flow conductivity of a CBM reservoir, a 3D geomechanical model of fractures development during volume fracturing was built with the MEYER software²². The model was used to study the influence of elastic modulus, horizontal principal stress difference, fracturing fluid viscosity and injection rate on the fracture network formed. Parameters used in the numerical simulation were based on the test results. The results can provide a reference basis for volume fracturing optimization design and productivity prediction analysis of CBM reservoirs.

Basic theory and algorithm

The governing mass conservation equation for incompressible slurry flow in a fracture is

$$\int_0^t q(t)dt - V_f(t) - V_1(t) - V_{sp}(t) = 0. \quad (7)$$

where t (s) is the time, q (m³/s) the injection flow rate, V_f , V_1 and V_{sp} (m³) are the fracture volume, fluid loss volume and volume loss by spurt respectively.

The mass continuity equation in terms of flow rate per unit length is

$$\bar{\nabla} \cdot \bar{q} + 2qL + (\partial W / \partial t) = 0, \quad (8)$$

where L (m) is the half-length of the fracture and W (m) is the fracture width.

The momentum equation (equation of motion) for steady flow is

$$\bar{\nabla} P = -(1/2)f\rho\bar{q}^2/w^3, \quad (9)$$

where P (Pa) is the pressure, f the Darcy friction factor and ρ (kg/m³) is the density of the fracturing fluid.

The crack-opening and opening pressure relationship is of the form²²

$$W(x, z, t) = \Gamma_w(x, y, z, t) \frac{2(1-\nu)}{G} H_\xi \Delta P(x, 0, t), \quad (10)$$

where x, y, z (m) are the coordinates of the given point, Γ_w is a generalized influence function, ν the Poisson ratio of the matrix, G (Pa) the shear modulus of the matrix, H_ξ (m) a characteristic half-height and ΔP (Pa) is the net fracture pressure.

The fracture propagation solution is obtained numerically by satisfying mass conservation (eq. (7)), continuity (eq. (8)), momentum (eq. (9)), elasticity relationship (eq. (10)) and fracture propagation criteria.

The governing differential equations for fracture propagation are differentiated with respect to time and then simplified to form a set of equations in terms of the alpha parameters

$$\alpha_\zeta = (t/\zeta)(d\zeta/dt).$$

α_ζ accounts for the time-dependent gamma parameters, non-steady injection rates and fluid rheology, spurt loss, fracture toughness, etc.

The length propagation parameter is of the form

$$\alpha_L = \frac{1 - \left(\alpha_c + \frac{1}{2} \right) (1 - \eta) + \alpha_c}{1 + \frac{\eta [1 + \beta_H (3 + n')]}{(1 + n') (1 - \beta_\lambda)}}, \quad (11)$$

where α_L is the length propagation parameter. α_c the leakoff parameter during pumping, η and β_H the fracture efficiency ($\beta_H = \alpha_H/\alpha_L$), n' the flow behaviour index and β_λ is the geometric factor which is equal to unity for the PKN and 3D type fracture models and is zero for the Geertsma and de Klerk (GDK) model.

Equation (11) and the formulated constitutive relationships control the time-dependent length propagation solution

$$L(t) = L(t_n) (t/t_n)^{\alpha_L(t)}. \quad (12)$$

where t_n (s) is the given time of hydraulic fracture.

Simulation model and analysis of results

The fracturing well JZ-B in Jiaozuo mining area has been selected as an example to carry out numerical simulation. Figure 12 shows its wellbore configuration. The parameters of the fracturing well production casing are as follows: external diameter and wall thickness 139.7 and 7.72 mm respectively. Steel grade is J55 and vertical

depth is 1120 m. On account of there being no tubing, we took casing fracturing pattern for simulation modelling. The top depth of the coal seam is 1069.5 m, and its thickness is 8.7 m. The vertical principal stress, and maximum and minimum principal stress in the coal seam are 23.4, 25.7 and 16.7 MPa respectively.

To ensure that the input parameters of the numerical model truly represent the actual formation, the average values of coal rock matrix and bedding determined in the laboratory tests were used as the mechanical parameters of the coal seam. Table 9 shows the mechanical parameters of coal seam and upper and lower strata.

For the fracturing well we adopted the casing perforation completion method to make the artificial fracture system communicate better with the natural fracture system. Table 10 shows the perforation parameters of the fracturing well.

Fracturing fluid mainly has the function of fracture forming, sand transportation and flow back, but the damage of natural fractures and bedding must be considered first.

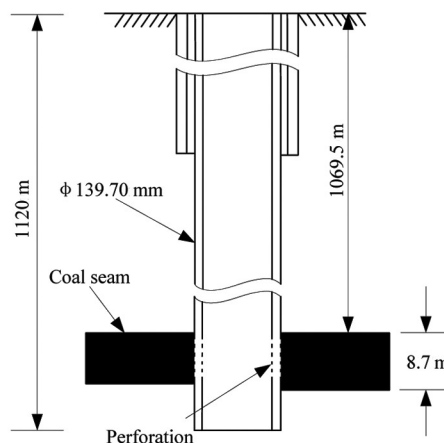


Figure 12. Wellbore configuration of fractured well.

Table 9. Mechanical parameters of coal seam and upper and lower strata

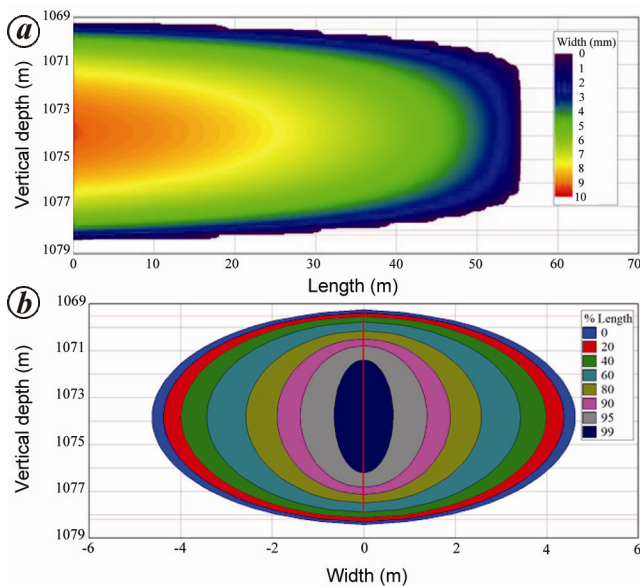
Lithology	Parameter	Value
Coal seam	Compressive strength (MPa)	7.47
	Elastic modulus (GPa)	1.29
	Poisson ratio	0.325
	Cohesive strength (MPa)	0.505
	Internal friction angle (°)	17.55
	Tensile strength (MPa)	0.72
	Fracture toughness (MPa m ^{0.5})	0.242
	Permeability (mD)	0.51
Upper and lower strata	Elastic modulus (GPa)	12.5
	Poisson ratio	0.32
	Cohesive strength (MPa)	3.2
	Internal friction angle (°)	30.5
	Tensile strength (MPa)	2.2
	Fracture toughness (MPa m ^{0.5})	1.2
	Permeability (mD)	0.002

Table 10. Perforation parameters of JZ-B well

Number of perforations	Perforation density (hole/m)	Perforation diameter (mm)	Perforation vertical depth (m)	Perforation length (m)
85	10	9.91	1069.5	8.5

Table 11. Proppant performance indicators

Parameter	Value
Roundness	0.67
Sphericity	0.68
Acid solubility (%)	2.9
Turbidity (NTU)	10.1
Breakage rate (%)	16.27
Screen analysis (%)	92.40

**Figure 13.** Major fracture geometry. *a*, Major fracture length profile. *b*, Major fracture width profile.

On account of the strong adsorption ability of coal, the fracturing fluid compatibility should be very high, otherwise adsorption or adverse reaction will take place between fracturing fluid and coal²⁶. Selection criteria of fracturing fluid are as follows: reduce fracturing fluid adsorption as far as possible, prevent cleat blockage, and the reservoir permeability remains constant. The characteristics of the fracturing fluid have a direct impact on fracture geometry and flow conductivity. Taking coal seam characteristics, fracturing technology and economic costs into consideration, we chose active water fracturing fluid in the fracturing well.

Proppant is also one of the key factors influencing the fracture flow conductivity, with a role to fill and support the hydraulic fracture, and form flow channels of high conductivity. Its performance directly affects yield-

increasing effect and production dynamics²⁷. In addition, the effect of turbulence on fracture conductivity capacity and the problem of fracturing fluid pollution must be considered. Propping agent is primarily quartz sand, with a density of 2650 kg/m³. Table 11 shows other performance indicators of proppant.

We must inject a large amount of high filtration and mild gel liquid through the fracturing well to expand natural fractures in CBM reservoirs. Fracturing fluid and proppant are injected into natural and artificial cracks to expand reservoir seepage area and increase production capacity. We adopted a constant injection rate of 15 m³/min. The injection time was 60 min. Table 12 presents other basic parameters used in the numerical simulation.

Fracture geometry after volume fracturing in CBM reservoir was simulated using MEYER. The results show that one can form an interconnected fracture network by volume fracturing in a CBM reservoir. Figures 13 and 14 show the main crack and fracture network geometry. Figure 13 *a* shows that the half-length, height and largest width of the main fracture are 55.41 m, 9.18 m and 9.25 mm respectively (in the figure, the fracture width range is from 0 to 10 mm from outside to inside). The closer to the wellbore, higher are the values of width and height. As shown in Figure 13 *b*, the width profile of the main crack is approximately an ellipse (the fracture width percentage is from 0 to 99 from outside to inside). The height and width decrease with crack length extension.

Figure 14 shows the crack network system after completion of injection. The coordinates origin of the *x*-*y* plane is the centre of the main fracture, the *x*-axis is along the length direction of the main crack and the *y*-axis is perpendicular to the main fracture along the secondary fracture propagation direction. Secondary cracks form a series of interlocking fractures centred on the main crack. The profile of the fracture network is approximately equal to the long axis of the main fracture. Volume fracturing results in 21 cracks, which indicates that it has a good effect on the CBM reservoir, and can greatly improve well production. Seven cracks are parallel to the *x*-axis. Secondary cracks are symmetrical about the main fracture. Fourteen secondary cracks are parallel to the *y*-axis and present a symmetrical distribution. The width profile shows that the fractures propagating parallel to the maximum horizontal stress (*x*-direction) have much larger apertures than those that propagate along the *y*-direction. Net pressure near the wellbore area is the largest, so it is most likely to produce main fracture and

Table 12. Other basic parameters used in the numerical simulation

Parameter	Value	Parameter	Value
Overall filtration coefficient ($\text{m min}^{0.5}$)	0.0001524	Spurt loss coefficient (m^3/m^2)	0.0012
Reservoir fluid viscosity (mPa s)	10	Proppant size (mm)	0.67
Wall building filtration coefficient ($\text{m min}^{0.5}$)	4.8	Fluid compressibility (1/MPa)	4.27×10^{-4}
Darcy friction factor	0.04	Fracturing fluid viscosity (mPa s)	1
Fracturing fluid density (kg/m^3)	1013		

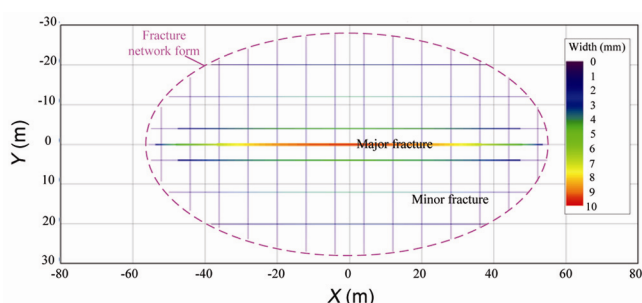


Figure 14. Fracture network.

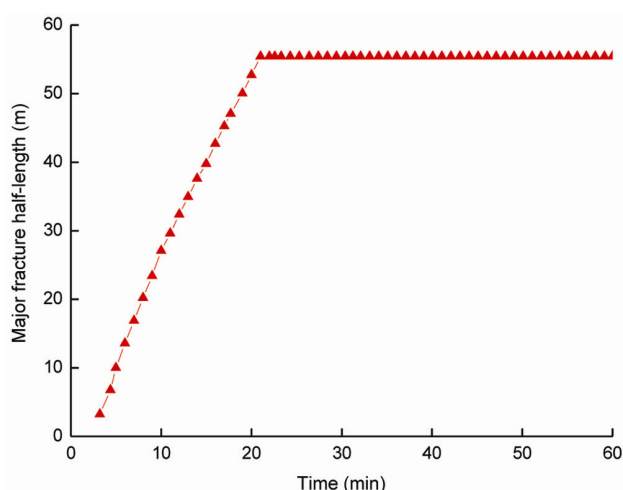


Figure 15. Main fracture half-length over time.

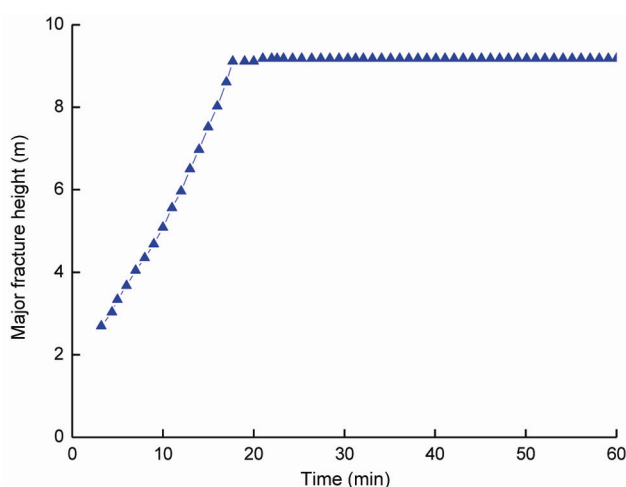


Figure 16. Main fracture height over injection time.

multiple secondary cracks. However, permeability along the y-axis is less so multiple high-flow conductivity cracks are parallel to the main fracture.

Figure 15 shows that the length of the main crack has an approximately linear relationship with injection time in early volume fracturing. The length reaches a maximum at 21.3 min, and then remains virtually constant.

Figure 16 shows the relationship between main fracture height and injection time. The height of the main crack has an approximately linear relationship with injection time early on. The height reaches a maximum value at 21.3 min; thereafter it shows no more obvious change.

As we can see from Figure 17, the maximum and average widths of the main fracture are small in early volume fracturing. These are 2.60 and 1.31 mm respectively at 21.3 min. Thereafter, the main fracture width grows rapidly and shows a linear relationship with injection time. At operating time 21.3 min, the crack width curve shows an inflection point. At the end of injection, the maximum and average widths reach 9.25 and 5.55 mm respectively.

Figure 18 shows the relation between the number of fractures and injection time. The number of cracks does not grow continuously, but presents jumps. The energy at the crack tip increases with injection time. New cracks are produced when the energy reaches a critical value, and then the stored energy is released. Fracturing fluid and propping agent enter the new fractures. New energy and bridging happen again in the crack tip, which leads to the formation of new secondary fractures. At the same time, the built-up energy can cause further extension of the crack size.

Influence factor analysis

Considering the numerous factors that influence the fracture geometry, we carried out a quantitative analysis of the fracture network on the basis of parameters such as elastic modulus, horizontal principal stress difference, fracturing fluid viscosity and injection displacement.

Elastic modulus

In order to study the effect of elasticity modulus on fracture network, we keep the other parameters constant. Table 13 shows the input elastic moduli and Figure 19 shows results of that calculation.

Figure 19 shows the fracture network for different elastic moduli. In the figure, the coordinate origin of the x - y plane is the midpoint of the main fracture. The x -axis (major axis) is parallel to and the y -axis (minor axis) is perpendicular to fracture length direction of the main crack. Secondary cracks form criss-crossed network systems centred on the main fracture. The fracture network geometry is approximately an ellipse. For case 1.1, nineteen cracks are produced. Seven cracks are parallel to the major axis, including the main fracture and 6 secondary cracks. There are secondary cracks along the minor axis. For case 1.2, 21 cracks are formed with 7 and 14 fractures parallel to the major and minor axes respectively. For case 1.3, there are 25 cracks, including 9 and 16 fractures along the major and minor axes respectively.

With an increase in coal elastic modulus, there is also an increase in the number of fractures and fracture area. This is because elastic modulus has a major influence on

the brittleness index. The greater the elasticity modulus, higher is the rock brittleness index and stronger is the fracture network forming ability. The length of the fracture increases with increasing elastic modulus.

Thus, the number of fractures and fracture area increase with the increase in coal elastic modulus. Li *et al.*¹⁴ pointed out that higher coal elastic modulus was beneficial in forming longer fractures in a coal seam. However, the fracture network geometry was not described. Similar analyses have been discussed in shale formations. According to Zou *et al.*²⁸, the elastic modulus of shale significantly influenced the fracture complexity and the stimulated reservoir volume. The fracture number and fracture area increased, while the average fracture width decreased with higher elastic modulus. Their conclusions are consistent with the results reported here.

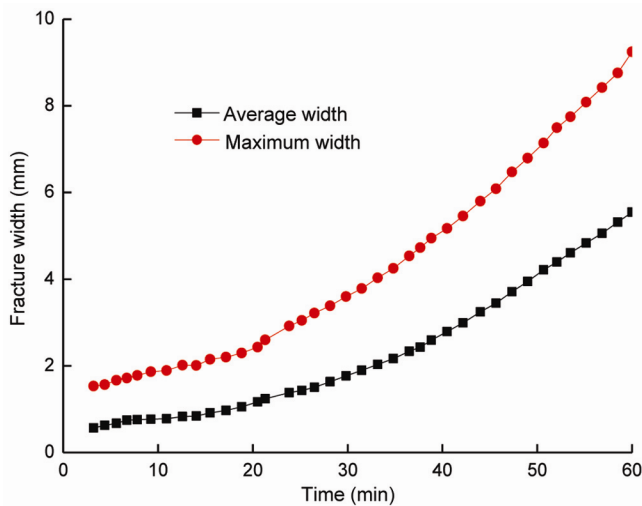


Figure 17. Main fracture width over injection time.

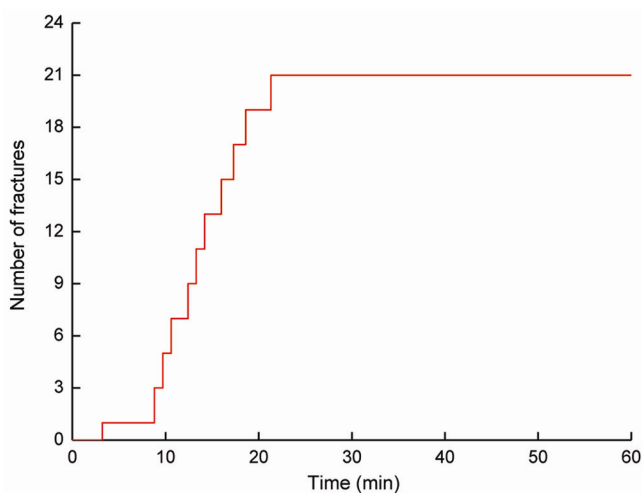


Figure 18. Number of fractures over time.

Table 13. Input elastic moduli for cases 1.1–1.3

Parameter	Cases		
	1.1	1.2	1.3
Elastic modulus (GPa)	0.79	1.29	1.79

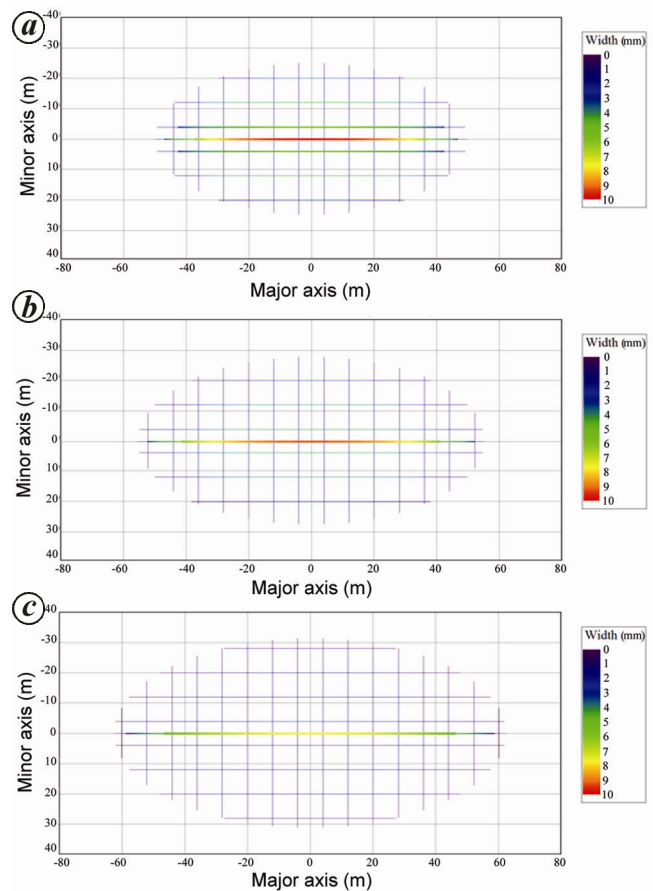


Figure 19. Fracture network for case 1.1 (a), case 1.2 (b) and case 1.3 (c).

Horizontal principal stress difference

In this section the effect of the horizontal principal stress difference on fracture network formed is studied. Table 14 shows the initial input parameters.

Figure 20 shows the final fracture network geometries of cases 2.1 to 2.3. As the horizontal principal stress

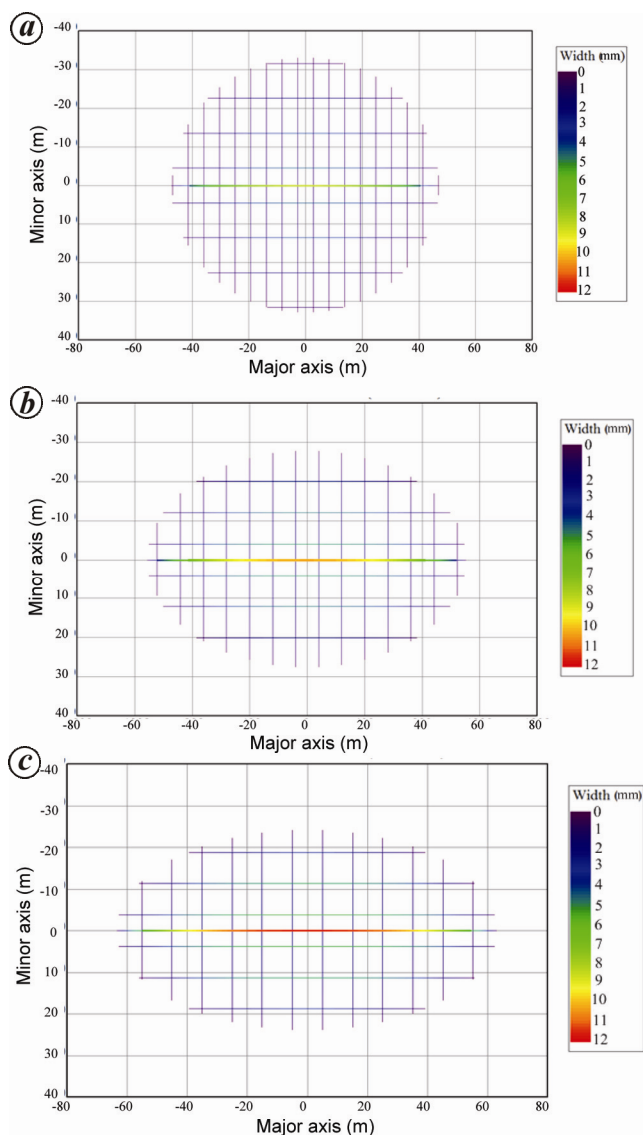


Figure 20. Fracture networks for cases 2.1 (a), case 2.2 (b) and case 2.3 (c).

Table 14. Input parameters for cases 2.1–2.3

Parameter	Case		
	2.1	2.2	2.3
Horizontal maximum principal stress (MPa)	22.7	25.7	28.7
Horizontal minimum principal stress (MPa)	16.7	16.7	16.7
Principal stress difference (MPa)	6	9	12

difference increases, the fracture network propagates further in the direction parallel to the maximum horizontal stress (major axis direction) but less so in the minor axis direction.

For case 2.1, there are 27 cracks with 9 and 18 fractures parallel to the major and minor axes respectively. For case 2.2, 21 cracks are produced with 7 and 14 fractures parallel to the major and minor axes respectively. For case 2.3, there are 19 cracks, including 7 and 12 fractures along the major axis and minor axes respectively.

Stress anisotropy has an adverse effect on the geometry of the fracture network in the CBM reservoir. The fracture number and fracture complexity decrease with larger horizontal stress difference. Li *et al.*¹⁴ proposed that the breakout pressure increased while the dimensions of the fracture increased when the vertical stress contrast between the barrier and the coal seam enlarged. The fracture network geometry in shale formations has been discussed. Zou *et al.*²⁸ argued that the hydraulic fracture geometry changed from a highly complex to a multi-branch network as the horizontal differential stress increased. Ahn *et al.*²⁹ also arrived at a similar conclusion. As maximum horizontal stress increased, fracture network propagated longer in the direction along the maximum horizontal stress, but less propagation occurred in the direction along the minimum horizontal stress. The change rules of fracture network agree well with the analysis results in the present study.

Fracturing fluid viscosity

In this section, the effect of fracturing fluid viscosity on fracture network geometry is studied. Table 15 shows the initial input parameters and Figure 21 shows results of calculation.

Figure 21 illustrates the final fracture network geometries of cases 3.1–3.3. As fracturing fluid viscosity increases, the fracture network propagates closer in the directions parallel to the major and minor axes.

For case 3.1, there are 17 fractures, with 7 and 10 cracks parallel to the major and minor axes respectively. For case 3.2, 21 cracks are formed with 7 and 14 fractures parallel to the major and minor axes respectively. For case 3.3, there are 27 fractures, including 9 and 18 along the major and minor axes respectively. With decreasing fracturing fluid viscosity, the number of fracture reduces greatly.

Table 15. Input parameters for cases 3.1–3.3

Parameter	Case		
	3.1	3.2	3.3
Fracturing fluid viscosity (mPa s)	0.5	1	10

From the above analysis, it can be seen that the fracture network propagates closer to the directions parallel to the major and minor axes, while the fracture number increase greatly with increasing fracturing fluid viscosity. Ahn *et al.*²⁹ proposed that the fracture geometries in shale formation showed significant differences due to differences in fracturing fluid viscosity. As fracturing fluid viscosity increased, the fracturing area decreased and the fracture width increased. The change laws of fracture network are in line with the results in this study.

Fracturing fluid injection rate

In this section the effect of fracturing fluid injection rate on fracture network geometry is described. Table 16

Table 16. Input parameters for cases 4.1–4.3

Parameter	Case		
	4.1	4.2	4.3
Total fluid rate (m ³)	900	900	900
Injection time (min)	90	60	45
Discharge capacity (m ³ /min)	10	15	20

shows the input parameters and Figure 22 shows results of the calculation.

Figure 22 shows the final fracture network geometries of cases 4.1–4.3. As fracturing fluid injection rate increases, the fracture network propagates closer to the directions of the major and minor axes. In the case of guaranteed crack extension, maintaining low injection rates is beneficial to the expansion of the fracture network.

For case 4.1, there are 19 fractures with 7 and 12 cracks parallel to major axis and minor axes respectively. For case 4.2, 21 cracks are formed with 7 and 14 fractures parallel to the major and minor axes respectively. For case 4.3, there are 21 fractures, including 9 and 16 fractures along the major and minor axes respectively. In conclusion, fracturing fluid injection rate has a major effect on the number of fractures induced in a CBM reservoir. The number of fractures increases with increasing fracturing fluid injection rate.

In conclusion, a higher injection rate enhanced the fracture number and fracture complexity, but decreased the fracture area and fracture network propagation distance along the directions of the major and minor axes. Li *et al.*¹⁴ proposed that the injection rate had a positive

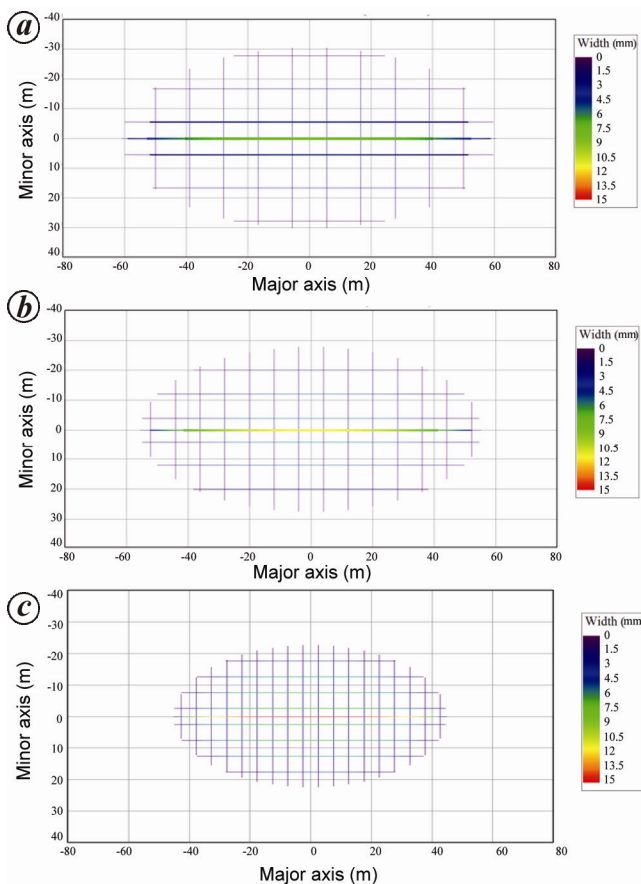


Figure 21. Fracture networks for case 3.1 (a), case 3.2 (b) and case 3.3 (c).

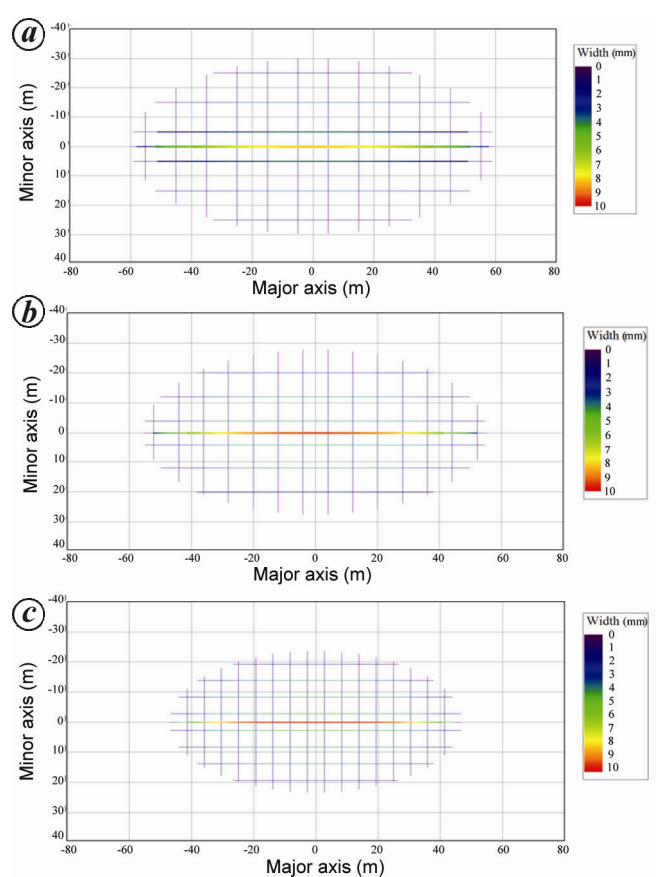


Figure 22. Fracture networks for case 4.1 (a), case 4.2 (b) and case 4.3 (c).

correlation with the three dimensions of the single hydraulic fracture in a CBM reservoir. Zou *et al.*²⁸ found that the higher injection rate raised the fluid pressure, which increased the potential of natural fracture opening and eventually the fracture complexity in shale formations. Ahn *et al.*²⁹ concluded that a longer but thinner fracture geometry was obtained when the injection rate was decreased. The conclusions of fracture network in shale formation were similar to the results in this study.

Conclusion

We carried out uniaxial and triaxial compression tests, Brazilian splitting test and three-point bending test on coal samples with different angles from the bedding planes. Compressive strength, elastic modulus, cohesive strength, tensile strength and fracture toughness of coal have obvious anisotropic characteristics. The brittle characteristics are significant during uniaxial compression. With an increase of confining pressure, the brittleness features weaken and coal samples suffer shear damage.

The dimensions of the main fracture are the largest in the fracture network during volume fracturing. Secondary fractures propagate more in the direction parallel to the maximum horizontal stress (major axis direction), and less in the minor axis direction, especially fracture length. The main fracture mainly extends along the crack length and width directions in the early volume fracturing. After a certain injection time the number of fractures does not grow continuously, but is discontinuous.

With an increase of coal elastic modulus, the number of fractures and fracture area increase, but crack width has an inverse relation with the modulus. Stress anisotropy has an adverse effect on geometry of the fracture network in CBM reservoir.

As fracturing fluid viscosity increases, the fracture network propagates closer to the directions parallel to major and minor axes. In the case of guaranteed crack extension, maintaining a low injection rate is beneficial to the expansion of the fracture network.

- Jiang, T. T., Yang, X. J., Yan, X. Z., Ding, Y. H., Wang, X. and Wang, T. T., Prediction of coalbed methane well production by analytical method. *Res. J. Appl. Sci. Eng. Technol.*, 2012, **4**(16), 2824–2830.
- Chong, H. A., Robert, D. and John, Y. W., Development of innovative and efficient hydraulic fracturing numerical simulation model and parametric studies in unconventional naturally fractured reservoirs. *J. Unconv. Oil Gas Resour.*, 2014, **8**, 25–45.
- Rao, C. S., Majumder, M., Roy, J., Chaudhari, M. S. and Ramteke, R. S., Delineating coal seams and establishing water tightness by electrical resistivity imaging. *Curr. Sci.*, 2015, **108**(3), 427–434.
- Jiang, T. T., Yang, X. J., Yan, X. Z., Ding, Y. H., Wang, X. and Wang, T. T., Numerical simulation of coalbed methane seepage in pinnate horizontal well based on multi-flow coupling model. *Res. J. Appl. Sci. Eng. Technol.*, 2012, **4**(16), 2881–2889.
- Jiang, T. T., Yang, X. J., Yan, X. Z., Ding, Y. H., Wang, X. and Wang, T. T., A study on numerical simulation of CBM pinnate horizontal well for near-wellbore seepage. *Res. J. Appl. Sci. Eng. Technol.*, 2012, **4**(22), 4791–4797.
- Su, Y. L., Ren, L., Meng, F. K., Xu, C. and Wang, W. D., Theoretical analysis of the mechanism of fracture network propagation with stimulated reservoir volume (SRV) fracturing in tight oil reservoirs. *PLOS ONE*, 2015, **10**(5), 1–25.
- Lian, Z. H., Yu, H., Lin, T. J. and Guo, J. H., A study on casing deformation failure multi-stage hydraulic fracturing for the stimulated reservoir volume of horizontal shale wells. *J. Nat. Gas Sci. Eng.*, 2015, **23**, 538–546.
- Cai, B. P., Liu, Y. H., Fan, Q., Zhang, Y. W., Liu, Z. K., Yu, S. L. and Ji, R. J., Multi-source information fusion based fault diagnosis of ground-source heat pump using Bayesian network. *Appl. Energ.*, 2014, **114**, 1–9.
- Jiang, T. T., Zhang, J. H. and Wu, H., Experimental and numerical study on hydraulic fracture propagation in coalbed methane reservoir. *J. Nat. Gas Sci. Eng.*, 2016, **35**, 455–467.
- Yang, C. H. *et al.*, Feasibility analysis of using abandoned salt caverns for large-scale underground energy storage in China. *Appl. Energ.*, 2015, **137**, 467–481.
- Medhurst, T. P. and Brown, E. T., A study of the mechanical behavior of coal for pillar design. *Int. J. Rock Mech. Min.*, 1998, **35**(8), 1087–1104.
- Misra, B. K., Singh, B. D. and Singh, A., Significance of coal petrological investigations in coal bed methane exploration-Indian context. *Curr. Sci.*, 2006, **91**(10), 1403–1409.
- Yuan, Z. G., Wang, H. T., Liu, N. P. and Liu, J. C., Simulation study of characteristics of hydraulic fracturing propagation of low permeability coal seam. *Disaster Adv.*, 2012, **5**(4), 717–720.
- Li, D. G., Zhang, S. C. and Zhang, S. A., Experimental and numerical simulation study on fracturing through interlayer to coal seam. *J. Nat. Gas Sci. Eng.*, 2014, **21**, 386–396.
- Xu, L. L., Cui, J. B., Huang, S. P., Tang, J. D., Cai, L. and Yu, P., Analysis and application of fracture propagated model by hydraulic fracturing in coal-bed methane reservoir. *Meitan J. China Coal Soc.*, 2014, **39**(10), 2068–2074.
- Klawitter, M., Esterle, J. and Collins, S., A study of hardness and fracture propagation in coal. *Int. J. Rock Mech. Min.*, 2015, **76**, 237–242.
- Li, Q. S. and Xing, H. L., Numerical analysis of the material parameter effects on the initiation of hydraulic fracture in a near wellbore region. *J. Nat. Gas Sci. Eng.*, 2015, **27**, 1597–1608.
- Kirk-Burnman, E., Pandey, V. J., Flottman, T. and Trubshaw, R. L., Hydraulic fracture design optimization in low permeability coals. In SPE Asia Pacific Unconventional Resources Conference and Exhibition, Brisbane, Australia, 9–11 November 2015.
- Dehghan, A. N., Goshtasbi, K., Ahangari, K. and Jin, Y., Mechanism of fracture initiation and propagation using a tri-axial hydraulic fracturing test system in naturally fractured reservoirs. *Eur. J. Environ. Civ. Eng.*, 2016, **20**(5), 560–585.
- Ma, S., Guo, J. C., Li, L. C., Xia, Y. J. and Yang, T., Experimental and numerical study on fracture propagation near open-hole horizontal well under hydraulic pressure. *Eur. J. Environ. Civ. Eng.*, 2016, **20**(4), 412–430.
- Zhang, G. Q., Chen, M., Liu, X., Zhao, W., Pu, X. and Yu, N., Relationship between rock compositions and mechanical properties of reservoir for low-permeability reservoirs. *Petrol. Sci. Technol.*, 2013, **31**(14), 1415–1422.
- Meyer, B. R., Heat transfer in hydraulic fracturing. *SPE Prod. Eng.*, 1989, **4**(4), 423–429.
- The geological and mineral of the People's Republic of China, *Rock Physical and Mechanical Properties test Procedures*, Geology Publishing House, Beijing, 1995.
- Ministry of Water Resources of the People's Republic of China, *Specifications for Rock Tests in Water Conservancy and Hydroelectric Engineering*, China Standards Press, Beijing, 2007.

-
25. Barbuta, M., Marin, E., Cimpeanu, S. M., Paraschiv, G., Lepadatu, D. and Bucur, R. D., Statistical analysis of the tensile strength of coal fly ash concrete with fibers using central composite design. *Adv. Mater. Sci. Eng.*, 2015, **2015**, 1–7.
26. Keck, R. G., Nehmer, W. L. and Strumolo, G. S., New method for predicting friction pressures and rheology of proppant laden fracturing fluids. *SPE Prod. Eng.*, 1992, **7**(1), 21–28.
27. Keshavarz, A., Badalyan, A., Carageorgos, T., Bedrikovetsky, P. and Johnson, R., Stimulation of coal seam permeability by micro-sized graded proppant placement using selective fluid properties. *Fuel*, 2015, **144**, 228–236.
28. Zou, Y. S., Zhang, S. C., Ma, X. F., Zhou, T. and Zeng, B., Numerical investigation of hydraulic fracture network propagation in naturally fractured shale formations. *J. Struct. Geol.*, 2016, **84**, 1–13.
29. Ahn, C. H., Dilmore, R. and Wang, J. Y., Development of innovative and efficient hydraulic fracturing numerical simulation model and parametric studies in unconventional naturally fractured reservoirs. *J. Unconv. Oil Gas Resour.*, 2014, **8**, 25–45.
- ACKNOWLEDGEMENTS. We acknowledge financial support through China Postdoctoral Science Foundation Funded Project (No. 2016M592402).
- Received 15 February 2016; revised accepted 10 August 2016
- doi: 10.18520/cs/v112/i02/332-347
-